



Constructing a continuous reduced graphene oxide network in porous plant fiber sponge for highly compressible and sensitive piezoresistive sensors

Gang Zhao¹ · Feng Qian² · Xinyi Li¹ · Yuhang Tang¹ · Ye Sheng³ · Handong Li^{4,5} · Jiuping Rao³ · Man Vir Singh⁶ · Hassan Algadi⁷ · Min Niu³ · Weijie Zhang¹ · Zhanhu Guo⁴ · Xiangfang Peng¹ · Tingjie Chen¹

Received: 11 May 2023 / Revised: 10 September 2023 / Accepted: 15 September 2023
© The Author(s) 2023

Abstract

Flexible pressure sensors as wearable electronic devices to monitor human health have attracted significant attention. Herein, a simple and effective carbonization-free method is proposed to prepare a compressible and conductive reduced graphene oxide (rGO)-modified plant fiber sponge (defined as rGO-PFS). The introduced GO can not only coat on the surface of plant fibers, but also form a large amount of aerogel with microcellular structure in the macroporous PFS. After reduction treatment, the rGO-PFS can form a double-continuous conductive network of rGO aerogel. With the improvement of polydimethylsiloxane (PDMS), the rGO-PFS@PDMS composite exhibits outstanding compressibility (up to 60% compression strain), excellent durability (10,000 stable compression cycles at 50% strain), high sensitivity (234.07 kPa^{-1} in a pressure range of 20–387.2 Pa), low detection limit (20 Pa), and rapid response time (28 ms) for practical wearable applications.

Keywords Plant fiber · Reduced graphene oxide · Sponge · Piezoresistive sensor · Wearable electronics

1 Introduction

With the prosperity of artificial intelligence and the improvement of living conditions, using flexible pressure/strain sensors as wearable electronics to monitor human health has aroused increasing attention [1–3]. Numerous pressure sensors made of metal and semiconductor show high sensitivity, fast response time, and excellent durability, but the

applications are still limited by their rigidity and small strain tolerance [4, 5]. Flexible pressure sensors with outstanding compressibility can meet various practical applications and can be classified into four types, i.e., piezoelectric, capacitive, triboelectric, and piezoresistive [6]. Piezoresistive sensor (PRS) that can transduce the external mechanical deformation into the resistance signal is a promising pressure sensor for preparing wearable electronics, attributing

Gang Zhao and Feng Qian contributed equally to this work.

✉ Zhanhu Guo
zhanhu.guo@northumbria.ac.uk

✉ Xiangfang Peng
pengxf@fjut.edu.cn

✉ Tingjie Chen
chentj@fjut.edu.cn

¹ College of Materials Science and Engineering, Key Laboratory of Polymer Materials and Products of Universities in Fujian, Fujian University of Technology, Fuzhou 350118, Fujian, China

² School of Automotive and Transportation Engineering, Wuhan University of Science and Technology, Wuhan 430081, Hubei, China

³ College of Transportation and Civil Engineering, College of Materials Science and Engineering, Fujian Agriculture and Forestry University, Fuzhou 350002, Fujian, China

⁴ Integrated Composites Laboratory (ICL), Department of Mechanical and Construction Engineering, Northumbria University, Newcastle Upon Tyne NE1 8ST, UK

⁵ College of Materials Science and Engineering, Taiyuan University of Science and Technology, Shanxi, Taiyuan 030024, China

⁶ Department of Chemistry, Dev Bhoomi Uttarakhand University, Dehradun 248007, India

⁷ Department of Electrical Engineering, College of Engineering, Najran University, Najran, Saudi Arabia

to its cost-efficient, simple fabrication process, and easy signal collection [7, 8]. In principle, excellent mechanical properties and reasonable electrical conductivity are very important when they are used as core components for fabricating flexible PRS devices [9, 10]. In the past few years, the PRS devices fabricated by combining various conductive materials [e.g., organics, carbon black, carbon nanotubes (CNT), metal nanowires/nanoparticles, and graphene and its derivatives] with the elastomeric polymers [e.g., polydimethylsiloxane (PDMS), silicon rubber, and polyurethane (PU)] and endowed with a designed structure (e.g., hollow-sphere and interlocked microstructures) via proper processing techniques have been widely investigated [11–17]. These devices with planar structures show excellent mechanical properties and high sensitivity, but their practical applications are still limited by the small detection range, tedious fabrication process, and poor stability [8, 18, 19].

It is worth noting that several key characteristics should be incorporated for an ideal PRS device with high sensitivity, such as high compressibility, low detection limits, broad detection range, and good fatigue resistance [9, 10, 20–23]. Compared to the planar structure, conductive porous materials with a continuous three-dimensional (3D) network structure are more suitable for fabricating the PRS devices, ascribing to their low density, high porosity, and good compression resilience. The existence of a porous structure is beneficial to decrease structural stiffness and remarkably improve the sensitivities and pressure regimes of PRS devices [21, 23–27]. The general strategy to construct conductive porous materials is using neat conductive materials (e.g., CNT, carbon nanofibers, conducting polymers, and graphene) through a specific technique (e.g., carbonization, template growth, vacuum freeze-drying, hydrothermal and thermal annealing treatment) [27–30]. For example, Weng et al. [29] prepared a conductive reduced graphene oxide (rGO) aerogel as a PRS device using the freeze-drying technique coupled with the reduction treatment. Zhang et al. [30] reported a PRS device based on the 3D porous graphene foam, which was prepared by chemical vapor deposition of the graphene on copper foam (as a template) followed by etching the copper skeleton. The PRS devices prepared using these porous materials show high sensitivity, but they still suffer from tedious fabrication processes and high production costs [6, 20, 27, 31, 32]. The other strategy to prepare the conductive porous materials as PRS devices is to fill the conductive materials into a 3D porous polymer via a simple and efficient dip-coating process. The prepared sponges simultaneously possess the electrical conductivity of conductive materials and the elasticity and compressibility of polymers. Especially, their conductivity can be controlled by adjusting the content of conductive materials [6, 20, 27, 33].

Until now, various kinds of conductive fillers (e.g., CNT, rGO, metallic nanoparticles and nanowires, carbon black

particles, and conductive polymers) have been used to modify the insulating polymer sponges (e.g., PDMS foam, thermoplastic PU foam, commercial PU and melamine sponges) [24, 34–37]. These cost-effective fabrications of conductive porous materials have been used to prepare the PRS devices, which show high sensitivity and excellent compressibility. Nevertheless, there are still some intractable problems hindering their applications, such as poor structural stability caused by the weak adhesion between the conductive materials and polymers and production of secondary pollution from the nondegradable polymer substrates [8, 18, 19].

Another strategy to prepare the conductive porous materials is carbonized biomass materials, which exhibits typical porous structures (e.g., vessel channels and pits) due to the transportation of water and nutrients for their photosynthesis [28, 38–41]. Numerous biomass-based materials have been used as sustainable carbon sources to create conductive porous materials, such as delignified wood [28], hydrothermally treated watermelon and winter melon [42], cotton fabric [43, 44], and cellulose/chitosan aerogel [45, 46]. The carbonized materials with satisfying conductivity can be directly used as a core component to fabricate the PRS devices, which can avoid tedious and environment-unfriendly problems [28]. However, due to the structural deformation during high-temperature carbonization, biomass-derived porous materials always show obvious brittleness and poor compression resilience. When directly applied to PRS devices, they cannot meet the requirements of applications in PRS accompanied by high-pressure sensitivity, excellent mechanical properties, and structural stability [43]. Considering that biomass materials are natural, low-cost, environmentally friendly, and renewable resources, their use as the carbon source to create 3D porous materials is still the mainstream research in flexible PRS. Consequently, developing a simple, cost-efficient, sustainable, and universal carbonization-free strategy is imperative to fabricate high-performance PRS based on natural biomass materials.

In this work, a simple and effective carbonization-free method was proposed to fabricate a compressible and conductive rGO-modified plant fiber sponge (defined as rGO-PFS), and its potential application in PRS with outstanding sensing performances was demonstrated. At first, plant fibers with numerous hydroxyl (-OH) groups were used as building blocks to construct a porous PFS through a convenient physical foaming strategy [47]. It is well known that low-cost and hydrophilic plant fibers are attractive for excellent mechanical strength and elasticity but electrically nonconductive [24, 48]. Owing to the unique structure, excellent mechanical properties, and high manipulability, GO aqueous dispersion was used to modify the PFS (defined as GO-PFS) by simple dip-coating and freeze-drying treatment. The introduction of GO can not only coat on the plant fibers' surface, but also form the continuous GO aerogels

with microcellular structure in the macroporous PFS. After reduction treatment, the electrically insulating GO-wrapped plant fibers and GO aerogels can be transformed into porous conductive materials, resulting in the formation of a double-continuous conductive network in rGO-PFS. With the improvement of PDMS, the flexible rGO-PFS@PDMS composite exhibited outstanding compressibility (up to 60% compression strain), excellent durability (10,000 stable compression cycles at 50% strain), high sensitivity (234.07 kPa^{-1} in a pressure range of $20 \sim 387.2 \text{ Pa}$), low detection limit (20 Pa), and rapid response time (28 ms). More importantly, rGO-PFS@PDMS-based PRS can be used to monitor human physiological signals, such as finger bending, knee movements, facial expression, phonation, and even pulse wave.

2 Experimental methods

2.1 Materials and chemicals

Kraft pulp was obtained from Tembec Inc., Canada. The chemicals of potassium permanganate (KMnO_4), sodium nitrate (NaNO_3), sulfuric acid (H_2SO_4), hydrogen peroxide (H_2O_2), hydrochloric acid (HCl), polyvinyl acetate (PVAc), sodium dodecyl benzene sulfonate (SDBS), PDMS, and dichloromethane were purchased from Sinopharm Chemical Regent Co., Ltd. (China). All of the components and chemicals were used as received without any additional purification.

2.2 Preparation of GO aqueous dispersion and rGO-PFS@PDMS

The GO aqueous dispersion was prepared using a modified Hummers' method [47]. First, the flake graphite was mixed with KMnO_4 and NaNO_3 under aggressive stirring. Then, the H_2SO_4 , H_2O_2 solution, and diluted HCl solution were successively added to the mixture. Finally, the resulting solution was washed several times with deionized (DI) water before being stored in a refrigerator for later use.

To prepare the PFS, 10 g of dry pulp fiber was defibered with 120 mL of DI water. Then, 5 g of PVAc emulsion and 5 mL of 10% aqueous SDBS solution were successively added to the pulp mixture with vigorous stirring for ~ 2 min. When the foam volume of the pulp mixture reached a designated value, it was poured into the prepared mold and dried in an oven at a temperature of 95°C for ~ 8 h. Following that, the obtained PFS were immersed into GO dispersion with different concentrations, including 3 mg mL^{-1} , 6 mg mL^{-1} , 9 mg mL^{-1} , and 12 mg mL^{-1} . When saturated with GO dispersion, the samples were taken out and freeze-dried for ~ 48 h to obtain GO-PFS. Then, GO-PFS was reduced in an oven at 195°C for ~ 2 h to obtain black rGO-PFS [49]. Finally, the rGO-PFS was treated with a 30 wt% PDMS/

dichloromethane solution via a simple dip-coating method and dried at 80°C for 30 min to prepare a compressible and conductive rGO-PFS@PDMS composite.

2.3 Characterization

The morphology of samples was carried out by scanning electron microscopy (SEM, Zeiss SIGMA), atomic force microscopy (AFM, Seiko Instrument), and transmission electron microscopy (TEM, TECNAI F-30). The chemical structure of samples was analyzed by an X-ray diffraction analyzer (XRD, X'Pert-Pro MPD, Philips-FEI) and a Raman spectrometer (DXR2xi). The thermogravimetric (TG) and differential TG (DTG) curves of samples were obtained from a thermogravimetric analyzer (TGA, NETZSCH STA 449F3). Fourier transform infrared spectrometer (FT-IR, Thermo Nicolet6700) was used to determine the chemical functional groups. The mechanical properties of samples were tested using a mechanical testing machine (UTM 2203). Additionally, the rGO-PFS@PDMS composite was sandwiched between two pieces of thin copper foils (as electrodes) to track their piezoresistive sensing performance by using the electrochemical workstation (CHI 760E) and digital bridge (TH 2830).

2.4 Finite element simulations

To offer a mechanistic understanding of rGO-PFS@PDMS, the deformation performance of PFS@PDMS with macroporous structure and rGO-PFS@PDMS with microcellular structure was simulated by finite element (FE) method. Both the PFS and rGO-PFS@PDMS modeling were meshed using the CPS4R, a 4-node bilinear plane stress quadrilateral element. The thickness of channel walls in PFS structural modeling was roughly kept the same as that of the curved layer in the rGO-PFS@PDMS structural modeling, while the same length diameter (20 length units), short diameter (10 length units), and thickness (2 length units) throughout the modeling was strictly maintained. The elastic properties of Young's modulus and Poisson ratio were set to 5 GPa and 0.2, respectively.

2.5 Human motion and sensory array detection

To demonstrate the application of rGO-PFS@PDMS as a wearable PRS device, it was cut into a rectangular solid with a size of $10 \times 10 \times 2 \text{ mm}^3$ and connected by copper foils. To monitor/collect human motions, it was fixed on a commercial woundplast and attached to certain body parts (e.g., face, neck, finger, arm, wrist, and knee). Here, a constant voltage of 3 V was applied to the sensor for piezoresistive sensing performance testing. The resistance changes caused by the various human motions were recorded by a digital bridge (TH 2830). Additionally, a 4×4 -pixel sensor array was prepared by mounting 16 pieces of rGO-PFS@PDMS

($10 \times 10 \times 2 \text{ mm}^3$) on a flexible polyethylene glycol terephthalate (PET) substrate to evaluate their tactile sensing capability. Each sensor in the sensor array was connected by copper tape as the common electrode. When a balance weight was placed on the sensor array's surface, their resistance changes were recorded in real time by the digital bridge.

3 Results and discussion

To use the nonconductive and environmentally friendly PFS as a porous frame material for fabricating a compressible and conductive porous material, a simple and effective carbonization-free method is proposed, including GO dispersion dipping/drying/reduction and PDMS dip-coating treatment (as shown schematically in Fig. 1). At first, the milk-white PFS with 3D network structure was prepared by the mechanical foaming strategy (Fig. 2a) [24]. The thin GO nanosheets ($\sim 1.5 \text{ nm}$ in thickness) in aqueous dispersion were prepared by the modified Hummers' method (Figs. S1, S2). Then, the PFS with numerous -OH groups were immersed into GO dispersion with different concentrations. Due to the existence of functional groups at the edge of GO nanosheets (e.g., -OH groups, epoxy groups, and carboxyl groups), the plant fibers can tightly adsorb GO nanosheets via the formation of hydrogen bonds and form a good connected interface (Fig. S3). When saturated with GO dispersion, the samples were taken out and freeze-dried to obtain GO-PFS. Notably, when the GO nanosheets were covered on plant fibers, the color of PFS changed from milk white to brown. After that, the GO-PFS was placed in an oven with a high temperature for thermal reduction treatment. When the functional groups were removed, a black and conductive rGO-PFS composite was obtained (Fig. 2a). To describe the interaction between plant fibers and GO

nanosheets, a possible intimate interaction mechanism was proposed and presented in Fig. 1b. Finally, the rGO-PFS was further encapsulated with a PDMS layer via a simple dip-coating method, resulting in a compressible and conductive rGO-PFS@PDMS composite. This method is simple and highly reproducible, where numerous rGO-PFS@PDMS ($\sim 0.08 \text{ g cm}^{-3}$) with a size of $6 \times 6 \times 2 \text{ cm}^3$ can be easily prepared (Fig. 2a).

As shown in Figs. 2b and S4, the PFS is composed of a hierarchical porous structure (ranging from tens of micrometers to hundreds of micrometers in size) as a result of the introduction of bubbles during the foaming. When the rGO nanosheets are introduced, the pore structure of rGO-PFS becomes more compact and uniform (Figs. 2c and S5). This is because the introduction of GO can form a large amount of aerogel filling in the porous structure of PFS, resulting in a continuous conductive network in rGO-PFS (Fig. 2d, e). The high-resolution SEM image shows each plant fiber is compactly coated by the rGO nanosheets, which is beneficial to promote the rapid electron transport for each plant fiber (Fig. 2f). More importantly, the rGO nanosheets perpendicular to the plant fibers are similar to a "screw thread," which may be beneficial for improving the sensitivity of rGO-PFS based PRS [20, 32]. To further confirm the reduction of GO nanosheets and the deposition of rGO in PFS, the TGA, DTG, FTIR, Raman, XRD, and XPS spectra were carried out. As shown in Fig. S6a, the total weight loss of PFS is as high as 78.3%, whereas the rGO-PFS is only 58.1%. The DTG curves show that the maximum decomposition peak of rGO-PFS is decreased from 335 to 300°C, ascribing to the reduction of GO on PFS (Fig. S6b). Compared to the FTIR spectrum of PFS, the wavenumbers of GO-PFS around 1750 cm^{-1} , 1640 cm^{-1} , and 1250 cm^{-1} are significantly increased, ascribing to the C=O stretching vibrations, C=C vibrations, and C-OH stretching vibrations, respectively (Fig. S7). In the FTIR spectrum of rGO-PFS, the intensity of C=O and C-OH stretching vibrations peak is decreased, where the intensity of C=C vibrations peak is further increased, attributing to the removal of the functional groups during the thermal reduction treatment [50]. The Raman spectra of GO-PFS and rGO-PFS clearly show the characteristic D-band ($\sim 1340 \text{ cm}^{-1}$) and G-band ($\sim 1580 \text{ cm}^{-1}$) of graphite, which are absent in the Raman spectra of PFS (Fig. 2g). It is worth noting that the I_D/I_G value of GO-PFS is increased from 0.83 to 1.04 (rGO-PFS), indicating the reduction of GO nanosheets to rGO nanosheets in PFS [36]. This phenomenon is also confirmed by the XRD measurements. In the XRD pattern of PFS, the peaks around 18.0° , 22.5° , and 35.0° can be ascribed to the characteristic (101), (002), and (040) peaks of fiber crystalline structure [51]. In contrast, an additional peak around 9.5° is clearly observed in the XRD pattern of GO-PFS, which can be ascribed to the characteristic peaks of GO

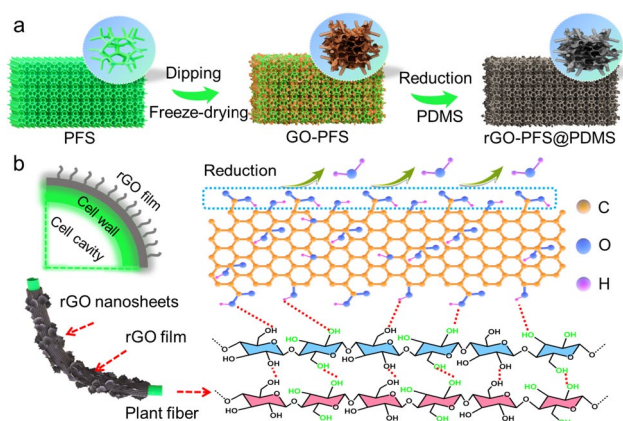


Fig. 1 **a** Schematic diagram shows the preparation of rGO-PFS@PDMS; **b** the possible reaction mechanisms between plant fibers and GO nanosheets

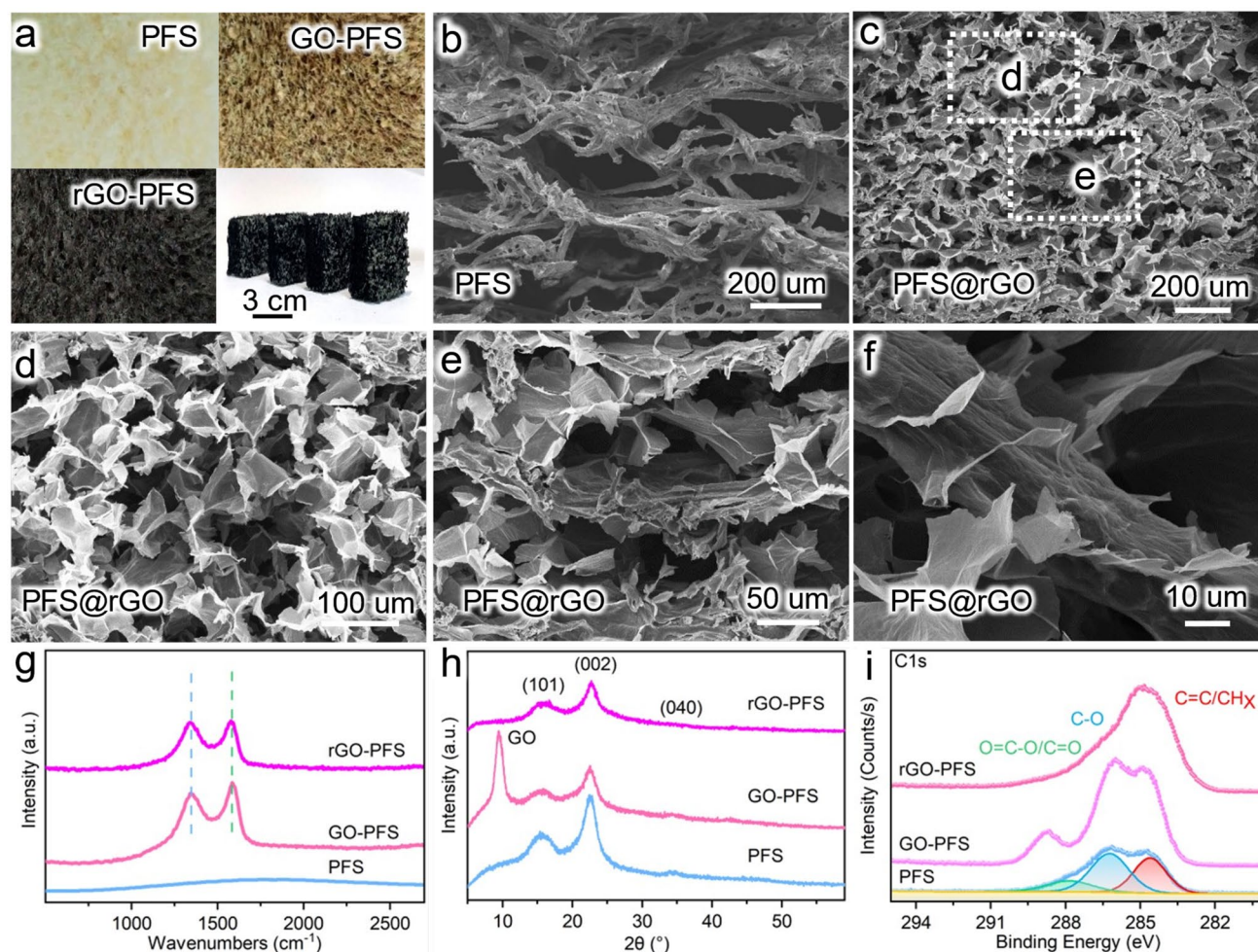


Fig. 2 **a** Optical images of PFS, GO-PFS, and rGO-PFS; **b** SEM image of PFS; **c–f** SEM images of rGO-PFS; **g** Raman spectra, **h** XRD spectra, and **i** XPS spectra of PFS, GO-PFS, and rGO-PFS

(Fig. 2h). When the GO-PFS is treated at high temperature, the characteristic peaks of GO disappear, demonstrating the reduction of GO in PFS. Furthermore, the surface chemical properties of PFS, GO-PFS, and rGO-PFS have been studied by XPS analysis (Fig. 2i). In the C1s spectrum of PFS, the peaks around 285 and 286.5 eV are corresponding to the C=C/CH_x and C-O groups, respectively. The intensity of the C=C/CH_x and C-O peaks in the C1s spectrum of GO-PFS are stronger than that of PFS. And an additional peak around 288.5 eV is clearly observed in the C1s spectrum of GO-PFS, which can be ascribed to the characteristic peaks of O=C–O/C=O groups. As expected, the peaks around 286.5 and 288.5 eV are disappearing after the reduction of GO-PFS. All the above results confirm that the GO nanosheets have deposited in the porous structure of PFS and been reduced into rGO nanosheets.

Considering that the piezoresistive sensing performance of rGO-PFS is directly affected by its structure and electrical conductivity, an important synthesis parameter of GO

dispersion concentration is optimized in this study. As shown in Fig. S8, the rGO-PFS treated by the various concentrations of GO dispersion shows a different conductivity. When GO dispersion is not used, the PFS shows a nonconductive composite. The rGO-PFS with a concentration of 3 mg mL⁻¹ exhibits only a low conductivity of ~0.52 μS cm⁻¹. This is because a loosened rGO porous structure is formed in PFS under the low GO dispersion concentration, resulting in the formation of a discontinuous conductive network (Fig. S9). With the increase in GO dispersion concentration, the conductivity of rGO-PFS dramatically increased. Here, the rGO-PFS with a GO dispersion concentration of 9 mg mL⁻¹ exhibits a relatively high conductivity of ~22.08 μS cm⁻¹. When the GO dispersion concentration exceeds 9 mg mL⁻¹, the conductivity of rGO-PFS can be increased. However, GO dispersion is difficult to penetrate the interior structure of PFS, which is deleterious to the compressibility and conductivity of rGO-PFS (Fig. S10). Consequently, the GO dispersion concentration used in this study is controlled to be 9 mg mL⁻¹.

Mechanical robustness with desirable compressibility is critical for sponge-like materials in PRS applications [10]. Benefiting from the construction of rGO microcellular structures in the macroporous PFS, the elastic rGO-PFS@PDMS composite demonstrates a favorable mechanical compressibility with a relatively high compressive strain (ε) of ~60%. As shown in Fig. 3a, rGO-PFS@PDMS can be repeatedly compressed and recover fast to its original height upon the release of applied loading, demonstrating its good elasticity. To evaluate the mechanical performance of rGO-PFS@PDMS more quantitatively, the corresponding compressive stress–strain (σ – ε) curves were measured under different applied ε ranging from 20 to 60% (Fig. 3b). Similar to most of reported sponge-like materials, the σ – ε curves of rGO-PFS@PDMS demonstrate three typical regions during the loading process: (1) a rather linear elastic region when $\varepsilon < 10\%$; (2) a plateau region within a ε

of 10–40%, attributing to the bending and buckling of the porous skeleton; (3) a nonlinear region with sharply increasing of σ when $\varepsilon > 40\%$, causing by the crushing of porous skeleton [28, 51]. In the release process, the rGO-PFS@PDMS can almost recover to its original shape without any remaining compressive stress. Even with a high compressive strain of 60%, the rGO-PFS@PDMS can still remain an intact structure and shows a relatively low σ of 148 kPa, indicating its good elastic compressibility [24]. Cyclic compression-release tests carried out at a ε of 50% show almost no plastic deformation in each cycle, whereas the PFS@PDMS shows an obvious plastic deformation, indicating the excellent structural stability of rGO-PFS@PDMS (Figs. 3c, d, and S11). The energy loss coefficient of PFS@PDMS calculated from each cycle decreases from the first cycle of 0.55 to the 10,000th cycle of 0.37. By contrast, the energy loss coefficient of rGO-PFS@PDMS only decreases from

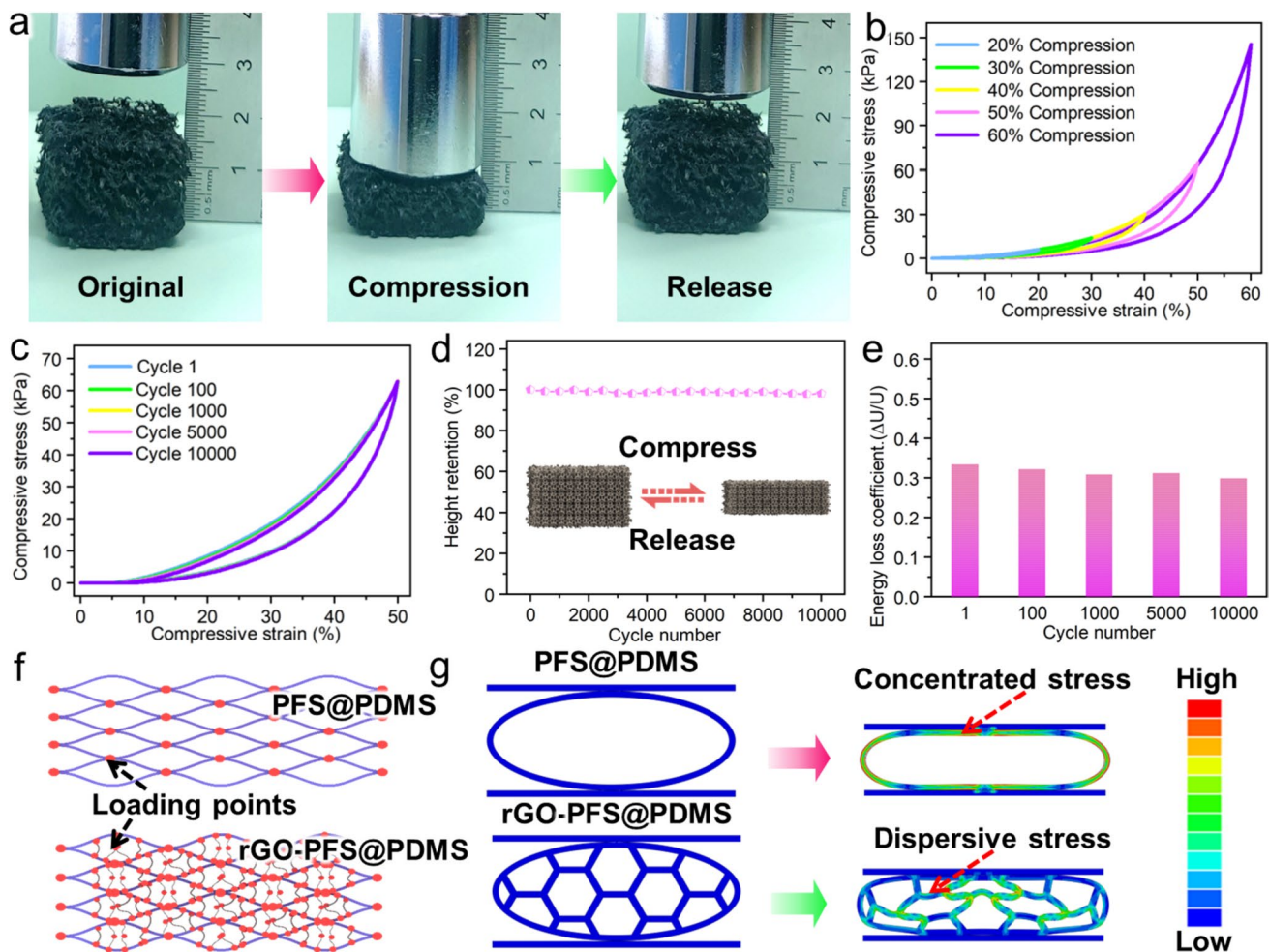


Fig. 3 Mechanical properties of rGO-PFS@PDMS: **a** optical images show the compression and recovery process; **b** compressive stress–strain curves at different strains; **c** compressive stress–strain curves of 1st, 100th, 1000th, 5000th, and 10,000th cycles at 50% strain; **d–e** Height retention and energy loss coefficient during 10,000 cycles at

50% strain; **f** schematic diagrams show the loading points of PFS@PDMS and rGO-PFS@PDMS; **g** stress distribution of PFS@PDMS and rGO-PFS@PDMS porous structure models in the compressive process simulated by the finite element analysis at a set strain of 50%

the first cycle of 0.33 to the 10,000th cycle of 0.29, which is superior to most of the reported sponge-like materials (Figs. 3e, S12, and Table S1) [24, 28, 51–56].

The improvement of mechanical property of rGO-PFS@PDMS can be ascribed to the construction of rGO microcellular structures in the macroporous PFS, which will provide more loading points to disperse the external stress than that of PFS (Fig. 3f). To offer a mechanistic understanding for the high compressibility of rGO-PFS@PDMS, a FE modeling is carried out to simulate the deformation performance of the rGO-PFS@PDMS with microcellular structure and compare it with that of PFS with macroporous structure. The simulated FE models were built based on the SEM images of the PFS (Fig. 2b) and rGO-PFS@PDMS (Fig. 2c). The simulation results show that the stress distribution of PFS@PDMS and rGO-PFS@PDMS is correlated with their structures. The stress of PFS@PDMS is mainly concentrated on the plant fibers' body and their joints (Fig. 3g). The stress concentration easily causes the severe deformation and collapse of the open macroporous structure, resulting in the permanent damage in the cellular walls at a large compressive loading and cannot be recovered upon the release of compressive loading. In comparison, the rGO-PFS@PDMS with microcellular structures show low stress on the plant fibers' body, where the stress is distributed on the whole porous structure body and reduced the stress concentration (Fig. 3g). The closely aligned rGO nanosheets in the internal structure are very tightly connected with the macroporous structure of PFS. When subjected to high compressive loading, the introduction of small rGO cells in PFS will disperse force under compression, resulting in a rather regulated and coordinated deformation of the cellular walls [20, 32]. The FE simulation results are in good agreement with the experimental observation and tests of rGO-PFS@PDMS.

It is well known that the resistance change ($\Delta R = R_0 - R$, where R_0 and R represent the resistance without and with applied stress) of porous materials is mainly caused by the deformation of their conductive networks under various external pressures. To make the rGO-PFS@PDMS usable as sensing materials for fabricating wearable and durable PRS devices, owning a sensitive conductive network and excellent piezoresistive sensitivity is also an indispensable parameter as well as excellent structural stability [9]. To evaluate the electrical conductivity and piezoresistive sensitivity of rGO-PFS@PDMS, it was assembled into a simplified flexible PRS device by sandwiching the rGO-PFS@PDMS with a pair of copper tapes. Then, this PRS device was connected in series with a LED light and a power supplier with an applied voltage of 3 V (Fig. 4a). As shown in Fig. 4b, the LED light shows almost no brightness without external pressure. With the increasing compressive strain, the brightness of the LED light gradually increases, owing to the increased conductivity of the rGO-PFS@PDMS sensor.

To optimize the piezoresistive performance, the rGO-PFS@PDMS sensor was prepared by changing the GO dispersion concentration of 6, 9, and 12 mg mL⁻¹. As shown in Fig. 4c, the rGO-PFS@PDMS sensor treated by a GO dispersion concentration of 9 mg mL⁻¹ shows the highest on/off resistance variation ratio [$\Delta R/R_0 = (R_0 - R)/R_0$], indicating an optimal porous structure and conductive network of rGO-PFS@PDMS. This result is consistent with the above-mentioned electrical conductivity optimization. As such, the optimal GO dispersion concentration of 9 mg mL⁻¹ is selected to fabricate the rGO-PFS@PDMS.

With the optimized preparation parameters, the rGO-PFS@PDMS shows a considerable resistance variation ratio. As shown in Fig. 4d, the $\Delta R/R_0$ of rGO-PFS@PDMS rapidly increased when it was subjected to an external pressure. The reduction of resistance is apparently caused by the increased amount of contact sites during compressive deformation in the microcellular structures of rGO-PFS@PDMS. In the compression process, the $\Delta R/R_0$ exhibits three different regions, including rapid increase region ($\epsilon < 5\%$), moderate response stage ($5\% < \epsilon < 10\%$), and relatively stable region ($\epsilon > 10\%$). Especially, the rGO-PFS@PDMS sensor shows a high $\Delta R/R_0$ of 90.6% at a small compression strain of 5%. Due to the excellent mechanical stability, the rGO-PFS@PDMS sensor can almost recover to its original state when the external pressure is removed. The rGO-PFS@PDMS sensor exhibits a high piezoresistive sensitivity, which can be defined as $Sp (\%) = (\Delta R/R_0)/\Delta P \times 100\%$ (ΔP represents the external pressure) [10]. As shown in Fig. 4e, the $\Delta R/R_0$ increases from a low pressure of 20 Pa, and the corresponding Sp exhibits two different regions. In the low-pressure region (< 387.2 Pa), the rGO-PFS@PDMS sensor shows a high sensitivity value of 234.07 kPa⁻¹, while only 0.01 kPa⁻¹ is obtained in the high-pressure region (> 387.2 Pa). Additionally, the rGO-PFS@PDMS sensor exhibits rapid response and recovery time of 28 ms and 76 ms, which are higher than that of many PRS devices reported previously (Figs. 4f and Table S2) [6, 8, 9, 20, 24, 26, 27, 31, 32, 57–61]. The high piezoresistive sensitivity, low detection limit, and rapid response time can be ascribed to the random distribution of numerous “screw thread” (rGO nanosheets) in the microcellular structures of rGO-PFS@PDMS. As shown in Fig. 4g, the rGO nanosheets can be mutually connected to each other via a “point-to-point” mode within a small ϵ ranging from 0 to 5%. As ϵ increases to 10%, the contact mode is changed into the “point-to-face,” resulting in the continuous reduction of resistance. When the ϵ further increases to 20%, the reduction of resistance is mainly relying on the typical “face-to-face” mode. Consequently, the rGO-PFS@PDMS with microcellular structure demonstrates an obvious $\Delta R/R_0$ and a high Sp at a low compressive strain.

As shown in Fig. 5a, the current–voltage (C–V) curves of the rGO-PFS@PDMS sensor under different

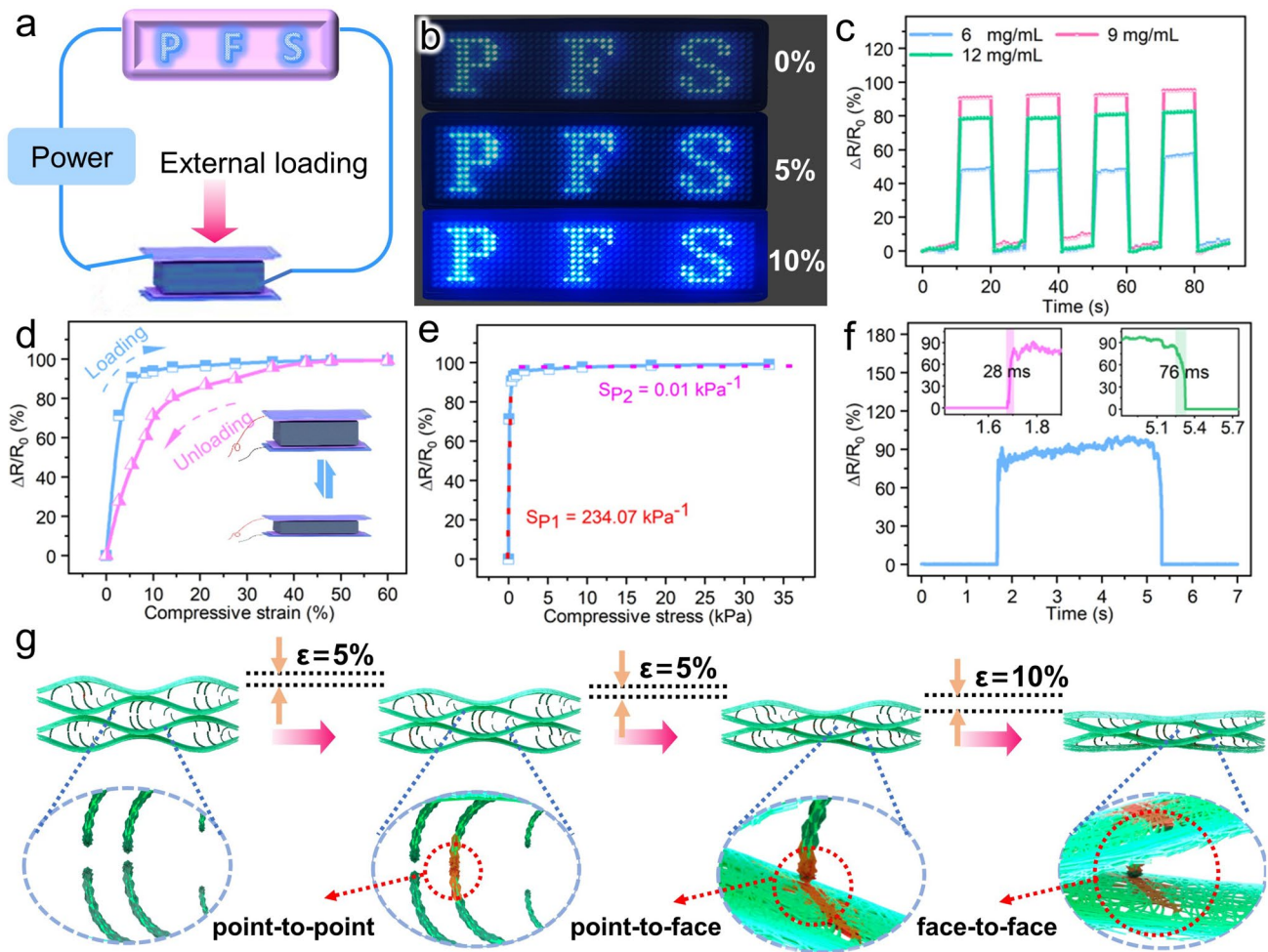


Fig. 4 **a–b** Diagram and photographs of the LED light with rGO-PFS@PDMS sensors under various compressive strains; **c** resistance change curves of the rGO-PFS@PDMS sensor with different GO dispersion concentration under constant pressures; **d–e** resistance change

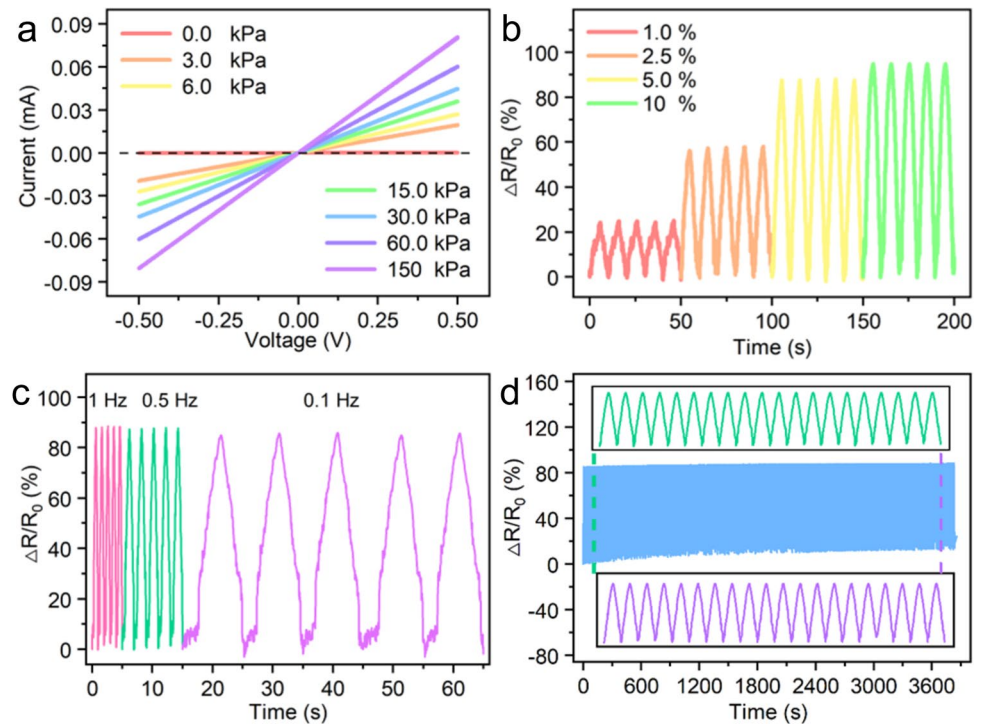
with respect to strain and pressure curves of rGO-PFS@PDMS sensors; **f** response time curves of rGO-PFS@PDMS sensors; **g** schematic diagrams show the structure changes of rGO-PFS@PDMS under different compressive strains

compression strains were carried out at voltage ranges from -0.5 to 0.5 V. All of the C-V curves show a good linear ohmic behavior, demonstrating the stable resistance characteristic of rGO-PFS@PDMS under constant pressure. When a constant frequency of 0.1 Hz is applied to the rGO-PFS@PDMS sensor, the various $\Delta R/R_0$ values can be collected under the different strains of 1% , 2.5% , 5% , and 10% . When the frequency is fixed, a stable $\Delta R/R_0$ value can be collected under a constant strain (Fig. 5b). Remarkably, the $\Delta R/R_0$ values can also be maintained under the different frequencies of 1.0 , 0.5 , and 0.1 Hz at a constant strain of 5% (Fig. 5c). Additionally, the $\Delta R/R_0$ values of rGO-PFS@PDMS sensor obtained from the 4000 cyclic compressing-releasing processes at a compression strain of 5% is used to evaluate its mechanical stability and durability. As shown in Fig. 5d, the $\Delta R/R_0$ values maintain a relatively stable level during the cyclic test, indicating a

stable signal output and can be a potential candidate for monitoring human physiological signals.

To demonstrate the practical application of rGO-PFS@PDMS as a wearable electronic, a tailored rGO-PFS@PDMS with a size of $10 \times 10 \times 2$ mm³ was fixed on a wound-plast as a PRS device. As shown in Fig. 6a, the rGO-PFS@PDMS-based PRS device is attached to the different parts of the human body surface for detecting various physiological signals, such as finger tap, finger/knee/wrist bending, cheek bulging, vocal vibration, and wrist pulse waves. This device shows no resistance change in the absence of any external pressure function (Fig. S13). When it is tapped by the finger, the uniform sharp peaks of $\Delta R/R_0$ signals caused by the structure deformation of rGO-PFS@PDMS during the repeated compressed processes can be precisely collected, indicating the good sensitivity and rapid response time of the PRS device (Fig. 6b). To collect the $\Delta R/R_0$ signals caused by

Fig. 5 **a** Current–voltage curves of rGO-PFS@PDMS sensors under various applied pressures. **b–d** Resistance variation under different strains at a frequency of 0.1 Hz, different frequencies at a compression strain of 5%, and 4000 continuous compressing-releasing cycles with a frequency of 1 Hz at 5% compression strain



the repeated finger bending, this device is also attached to the finger joint. When the finger is bent, the structure deformation will be produced by the bending of the PRS device, which will change its resistance. As shown in Fig. S14, a gradient increase of $\Delta R/R_0$ signals can be clearly observed with the increasing of finger bending angles. It is worth noting that a constant $\Delta R/R_0$ value corresponding to specific finger bending angles (e.g., 0°, 30°, 45°, 60°, and 90°) and a highly repeatable $\Delta R/R_0$ value during the repeated straightening and bending with constant finger bending angles (e.g., ranging from 0° to 45° and ranging from 0 to 90°) can be precisely collected by the device (Fig. 6c). Additionally, the repeatable and rapid $\Delta R/R_0$ signals caused by the repeated straightening and bending of others human body parts (e.g., knee and wrist joints) can also be precisely collected, indicating that the rGO-PFS@PDMS sensor can be used for real-time and dynamic human motion detection (Fig. 6d, e).

Due to the high piezoresistive sensitivity and low detection limit, the PRS device can be further used to collect the faint output signals obtained from tiny human motions. For example, when attaching the device to the human face, the repeatable $\Delta R/R_0$ signals can be clearly detected from the facial expression caused by the repeated cheek bulging (Fig. 6f). The distinct and repeatable signals produced by the speaking of different words (e.g., “A”, and “Carbon”) can also be detected after attaching the device to the human throat, indicating the potential application of the device in phonetic recognition (Fig. 6g). More

importantly, the device can be attached to the human wrist for pulse waveform detection. As shown in Fig. 6h, the distinct and regular waveform signals produced by wrist pulses are recorded with a normal waveform periodicity of $\sim 68 \text{ beats min}^{-1}$. The shape of pulse waveform curves collected by the device is consistent with the reported PRS devices and shows three typical characteristic peaks of percussion wave (P), tidal wave (T), and diastolic wave (D) [20]. Results indicate that the rGO-PFS@PDMS sensor is a promising wearable electronic device for real-time human health monitoring.

To further demonstrate the practical application, the rGO-PFS@PDMS sensor is connected in series with an AVO meter (OW18E) containing a Bluetooth system for real-time output signals collection (Fig. S15). As shown in Fig. S16, the real-time $\Delta R/R_0$ signals can be detected by the AVO meter and rapidly received and displayed on the phone through the Bluetooth system. Additionally, to demonstrate the tactile sensing applications, a pressure sensor array was fabricated by fixing 16 pieces of rGO-PFS@PDMS ($10 \times 10 \times 2 \text{ mm}^3$) onto a flexible PET substrate with a 4×4 -pixel array as a flexible multi-touch device (Fig. S17). As shown in Fig. S18, the 3D resistance variation signals' mapping corresponding to the surface pressure distribution is clearly recorded by the sensory array after placing various balance weights on its surface, demonstrating the potential application of the rGO-PFS@PDMS sensor in tactile sensing and human–machine interaction systems.

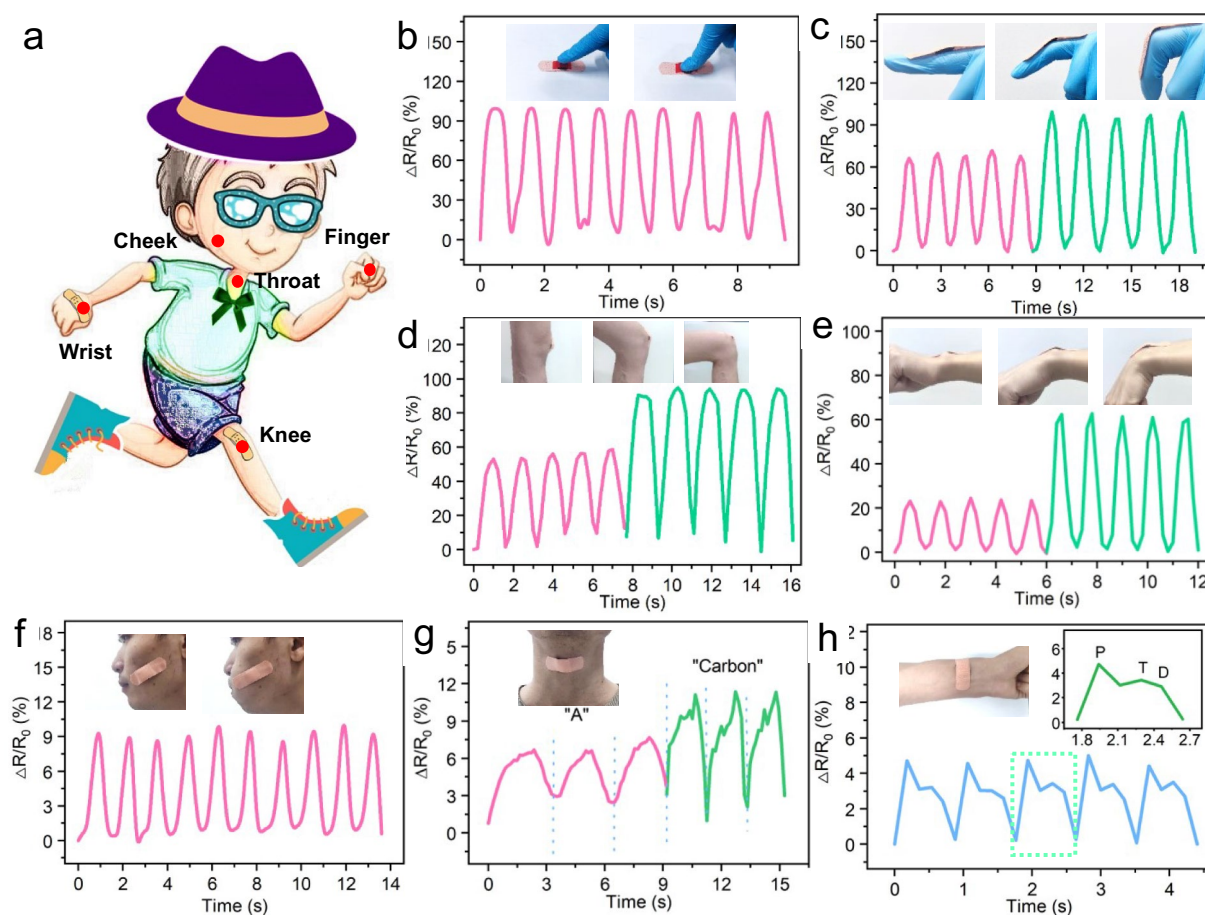


Fig. 6 **a** Schematic diagram shows the rGO-PFS@PDMS sensor attached to the different target parts of body for real-time detection; **b–h** real-time

resistance variation response to the human motions of finger tap, finger/knee/wrist bending, cheek bulging, vocal vibration, and wrist pulse waves

4 Conclusions

In summary, a simple and effective carbonization-free method is proposed to prepare a highly compressible and conductive rGO-PFS@PDMS as wearable PRS devices. Owing to the introduction of rGO aerogel with microcellular structure in the macroporous PFS and the encapsulation of PDMS, the rGO-PFS@PDMS composites with a double-continuous conductive network exhibit outstanding compressibility (up to 60% compression strain), excellent durability (10,000 stable compression cycles at 50% strain), high sensitivity (234.07 kPa^{-1} in a pressure range of 20–387.2 Pa), low detection limit (20 Pa), and rapid response time (28 ms). Consequently, the rGO-PFS@PDMS can be used as PRS devices for monitoring human physiological signals, such as finger bending, knee movements, facial expression, phonation, and even pulse waves. The fabricated method used in this work provides a new route to design and prepare biomass porous materials, which shows the great potential for practical application in wearable electronics.

Supplementary Information The online version contains supplementary material available at <https://doi.org/10.1007/s42114-023-00754-w>.

Author contribution Gang Zhao: Conceptualization, Methodology, Software, Writing-Original Draft, Data Curation. Feng Qian: Conceptualization, Methodology, Data Curation. Xinyi Li: Software, Writing-Original Draft, Investigation. Yuhang Tang: Software, Writing-Original Draft, Data Curation. Ye Sheng: Software, Data Curation. Handong Li: Format analysis, Writing-Original Draft. Jiuping Rao: Validation, Visualization. Man Vir Singh: Data Analysis. Hassan Algadi: Data Curation, Writing-Original Draft. Min Niu: Validation, Methodology. Weijie Zhang: Software, Data Curation. Zhanhu Guo: Supervision, Methodology, Writing-Original Draft. Xiangfang Peng: Project administration, Supervision. Tingjie Chen: Project administration, Conceptualization, Methodology, Data Curation, Supervision.

Funding The authors are thankful to the Deanship of Scientific Research at Najran University, Najran, Kingdom of Saudi Arabia, for funding this work, under the Research Collaboration funding program Grant No. NU/RG/SERC/12/10. The authors also received funding from the National Natural Science Foundation of China (52273032), Natural Science Foundation of Fujian Province (2020J05187 and 2020J02007), Scientific Research Foundation of Fujian University of Technology (GY-Z19084, GY-Z21014, and GY-Z17073), Science and Technology Program of Fujian Province (Regional Development Program, 2021N3003), Young and Middle-Aged Teacher Education

Research Project of Fujian Province (JAT200101), and College Students' Innovation and Entrepreneurship Training Program of Fujian University of Technology (S202110388043).

Data availability The data will be available upon proper request.

Declarations

Competing interests The authors declare no competing interests.

Open Access This article is licensed under a Creative Commons Attribution 4.0 International License, which permits use, sharing, adaptation, distribution and reproduction in any medium or format, as long as you give appropriate credit to the original author(s) and the source, provide a link to the Creative Commons licence, and indicate if changes were made. The images or other third party material in this article are included in the article's Creative Commons licence, unless indicated otherwise in a credit line to the material. If material is not included in the article's Creative Commons licence and your intended use is not permitted by statutory regulation or exceeds the permitted use, you will need to obtain permission directly from the copyright holder. To view a copy of this licence, visit <http://creativecommons.org/licenses/by/4.0/>.

References

- Balakrishnan A, Medikonda J, Namboothiri PN, Natarajan M (2022) Role of wearable sensors with machine learning approaches in gait analysis for Parkinson's disease assessment: a review. *Eng Sci* 19:5–19
- Li T, Wei H, Zhang Y, Wan T, Cui D et al (2023) Sodium alginate reinforced polyacrylamide/xanthan gum double network ionic hydrogels for stress sensing and self-powered wearable device applications. *Carbohydr Polym* 309:120678
- Shen Y, Yang W, Hu F, Zheng X, Zheng Y, Liu H, Algadi H, Chen K (2023) Ultrasensitive wearable strain sensor for promising application in cardiac rehabilitation. *Adv Compos Hybrid Mater* 6:21
- Gong S, Schwalb W, Wang Y, Chen Y, Tang Y, Si J et al (2014) A wearable and highly sensitive pressure sensor with ultrathin gold nanowires. *Nat Commun* 5:3132
- Yu R, Pan C, Chen J, Zhu G, Wang ZL (2013) Enhanced performance of a ZnO nanowire-based self-powered glucose sensor by piezotronic effect. *Adv Funct Mater* 23(47):5868–5874
- Yue Y, Liu N, Liu W, Li M, Ma Y, Luo C et al (2018) 3D hybrid porous MXene-sponge network and its application in piezoresistive sensor. *Nano Energy* 50:79–87
- Sheng L, Liang Y, Jiang L, Wang Q, Wei T, Qu L et al (2015) Bubble-decorated honeycomb-like graphene film as ultrahigh sensitivity pressure sensors. *Adv Funct Mater* 25(41):6545–6551
- Wang H, Li Y, Wang X, Liu Z, Ahmed M, Zeng C (2021) Preparation and characterization of piezoelectric foams based on cyclic olefin copolymer. *Eng Sci* 16:203–210
- Chen Z, Zhuo H, Hu Y, Lai H, Liu L, Zhong L et al (2020) Wood-derived lightweight and elastic carbon aerogel for pressure sensing and energy storage. *Adv Funct Mater* 30(17):1910292
- Su Y, Han G, Kong Z, Nantung T, Lu N (2020) Embeddable piezoelectric sensors for strength gain monitoring of cementitious materials: the influence of coating materials. *Eng Sci* 11:66–75
- He Y, Zhou M, Mahmoud M, Lu X, He G, Huang M, Elnaggar A, Lei Q, Liu H, Liu C, Azab I (2022) Multifunctional wearable strain/pressure sensor based on conductive carbon nanotubes/silk nonwoven fabric with high durability and low detection limit. *Adv Compos Hybrid Mater* 5:1939–1950
- Chen YF, Li J, Cai JH, Tan YJ, Tang XH, Liu JH et al (2019) Negative liquid sensing effect and tunable piezoresistive sensitivity in polydimethylsiloxane/carbon nanotubes/water-absorbing-expansion particles nanocomposites. *Compos Part A: Appl Sci Manuf* 126:3530
- Tan C, Dong Z, Li Y, Zhao H, Huang X, Zhou Z et al (2020) A high performance wearable strain sensor with advanced thermal management for motion monitoring. *Nat Commun* 11(1):3530
- Wu Q, Qiao Y, Guo R, Naveed S, Hirtz T, Li X et al (2020) Triode-mimicking graphene pressure sensor with positive resistance variation for physiology and motion monitoring. *ACS Nano* 14(8):10104–10114
- Kong D, El-Bahy Z, Algadi H, Li T, El-Bahy S, Nassan M, Li J, Faheim A, Li A, Xu C, Huang M, Cui D, Wei H (2022) Highly sensitive strain sensors with wide operation range from strong MXene-composited polyvinyl alcohol/sodium carboxymethyl-cellulose double network hydrogel. *Adv Compos Hybrid Mater* 5:1976–1987
- Wu Y, Liu J, Lin S, Huang K, Chen E, Huang K, Lei M (2022) New pressure matrix array sensor composed of flexible mechanical sensor elements. *Eng Sci* 18:105–112
- Zhu GJ, Ren PG, Wang J, Duan Q, Ren F, Xia WM et al (2020) A highly sensitive and broad-range pressure sensor based on polyurethane mesodome arrays embedded with silver nanowires. *ACS Appl Mater Interfaces* 12(17):19988–19999
- Chen J, Zhu Y, Chang X, Pan D, Song G, Guo Z, Naik N (2021) Recent progress in essential functions of soft electronic skin. *Adv Funct Mater* 31:2104686
- Zhang D, Zhang M, Wang J, Sun H, Liu H, Mi L, Liu C, Shen C (2022) Impedance response behavior and mechanism study of axon-like ionic conductive cellulose-based hydrogel strain sensor. *Adv Compos Hybrid Mater* 5:1812–1820
- Li L, Cheng Y, Cao H, Liang Z, Liu Z, Yan S et al (2022) MXene/rGO/PS spheres multiple physical networks as high-performance pressure sensor. *Nano Energy* 95:106986
- Liu S, Wu X, Zhang D, Guo C, Wang P, Hu W et al (2017) Ultrafast dynamic pressure sensors based on graphene hybrid structure. *ACS Appl Mater Interfaces* 9(28):24148–24154
- Tewari A, Gandla S, Bohm S, McNeill CR, Gupta D (2018) Highly exfoliated MWNT-rGO Ink-wrapped polyurethane foam for piezoresistive pressure sensor applications. *ACS Appl Mater Interfaces* 10(6):5185–5195
- Yao HB, Ge J, Wang CF, Wang X, Hu W, Zheng ZJ et al (2013) A flexible and highly pressure-sensitive graphene-polyurethane sponge based on fractured microstructure design. *Adv Mater* 25(46):6692–6698
- Chen T, Zhang X, Hu X, Wu Z, Cao F, Wang X et al (2020) Sensitive piezoresistive sensors using ink-modified plant fiber sponges. *Chem Eng J* 401:126029
- Pang Y, Tian H, Tao L, Li Y, Wang X, Deng N et al (2016) Flexible, highly sensitive, and wearable pressure and strain sensors with graphene porous network structure. *ACS Appl Mater Interfaces* 8(40):26458–26462
- Si Y, Wang X, Yan C, Yang L, Yu J, Ding B (2016) Ultralight biomass-derived carbonaceous nanofibrous aerogels with superelasticity and high pressure-sensitivity. *Adv Mater* 28(43):9512–9518
- Cheng Y, Ma Y, Li L, Zhu M, Yue Y, Liu W et al (2020) Bioinspired microspines for a high-performance spray $Ti_{(3)}C_{(2)}T_{(x)}$ MXene-based piezoresistive sensor. *ACS Nano* 14(2):2145–2155
- Chen C, Song J, Zhu S, Li Y, Kuang Y, Wan J et al (2018) Scalable and sustainable approach toward highly compressible, anisotropic, lamellar carbon sponge. *Chem* 4(3):544–554
- Weng B, Ding A, Liu Y, Diao J, Razal J, Lau KT et al (2016) Hierarchical nafen enhanced carbon aerogels for sensing applications. *Nanoscale* 8(6):3416–3424

30. Zhang D, Jiang C, Liu J, Cao Y (2017) Carbon monoxide gas sensing at room temperature using copper oxide-decorated graphene hybrid nanocomposite prepared by layer-by-layer self-assembly. *Sensor Actuat B-Chem* 247:875–882
31. Wu Y, Wu J, Lin Y, Liu J, Pan X, He X, Bi K, Lei M (2023) Melamine sponge skeleton loaded organic conductors for mechanical sensors with high sensitivity and high resolution. *Adv Compos Hybrid Mater* 6:4
32. Ma Y, Yue Y, Zhang H, Cheng F, Zhao W, Rao J et al (2018) 3D synergistical MXene/reduced graphene oxide aerogel for a piezoresistive sensor. *ACS Nano* 12(4):3209–3216
33. Xie W, Yao F, Gu H, Du A, Lei Q, Naik N, Guo Z (2022) Magnetoresistive and piezoresistive polyaniline nanoarrays in-situ polymerized surrounding magnetic graphene aerogel. *Adv Compos Hybrid Mater* 5:1003–1016
34. Hu Y, Zhuo H, Luo Q, Wu Y, Wen R, Chen Z et al (2019) Biomass polymer-assisted fabrication of aerogels from MXenes with ultrahigh compression elasticity and pressure sensitivity. *J Mater Chem A* 7:10273–10281
35. Liu J, Chen E, Wu Y, Yang H, Huang K, Chang G et al (2022) Silver nanosheets doped polyvinyl alcohol hydrogel piezoresistive bifunctional sensor with a wide range and high resolution for human motion detection. *Adv Compos Hybrid Mater* 5(2):1196–1205
36. Wei H, Li A, Kong D, Li Z, Cui D, Li T et al (2021) Polypyrrole/reduced graphene aerogel film for wearable piezoresistive sensors with high sensing performances. *Adv Compos Hybrid Mater* 4(1):86–95
37. Wu Y, Chen E, Weng X, He Z, Chang G, Pan X et al (2022) Conductive polyvinyl alcohol/silver nanoparticles hydrogel sensor with large draw ratio, high sensitivity and high stability for human behavior monitoring. *Eng Sci* 18:113–120
38. Ruan J, Chang Z, Rong H, Alomar T, Zhu D, AlMasoud N et al (2023) High-conductivity nickel shells encapsulated wood-derived porous carbon for improved electromagnetic interference shielding. *Carbon* 213:118208
39. Kang F, Jiang X, Wang Y, Ren J, Xu B, Gao G, Huang Z, Guo Z (2023) Electron-rich biochar enhanced Z-scheme heterojunctioned bismuth tungstate/ bismuth oxydide removing tetracycline. *Inorg Chem Front* in press. <https://doi.org/10.1039/D3QI01283B>
40. Wang Z, Yin K, Zhang Y, Sun K, Xie L, Cong M, Lei Y, Li X, Fan R (2022) Two-dimensional $Ti_3C_2T_x$ /carbonized wood metacomposites with weakly negative permittivity. *Adv Compos Hybrid Mater* 5:2369–2377
41. Vijeata A, Chaudhary G, Umar A, Chaudhary S (2021) Distinctive solvatochromic response of fluorescent carbon dots derived from different components of Aegle Marmelos Plant. *Eng Sci* 15:197–209
42. Li Y-Q, Samad YA, Polychronopoulou K, Alhassan SM, Liao K (2014) Carbon aerogel from winter melon for highly efficient and recyclable oils and organic solvents absorption. *ACS Sustain Chem Eng* 2(6):1492–1497
43. Li Y, Samad YA, Liao K (2015) From cotton to wearable pressure sensor. *J Mater Chem A* 3(5):2181–2187
44. Zhang M, Wang C, Wang H, Jian M, Hao X, Zhang Y (2017) Carbonized cotton fabric for high-performance wearable strain sensors. *Adv Funct Mater* 27(2):1604795
45. Gao HL, Zhu YB, Mao LB, Wang FC, Luo XS, Liu YY et al (2016) Super-elastic and fatigue resistant carbon material with lamellar multi-arch microstructure. *Nat Commun* 7:12920
46. Zeng Z, Wang C, Siqueira G, Han D, Huch A, Abdolhosseinzadeh S et al (2020) Nanocellulose-MXene biomimetic aerogels with orientation-tunable electromagnetic interference shielding performance. *Adv Sci* 7(15):2000979
47. Chen T, Wang S, Wu Z, Wang X, Peng J, Wu B et al (2018) A cake making strategy to prepare reduced graphene oxide wrapped plant fiber sponges for high-efficiency solar steam generation. *J Mater Chem A* 6(30):14571–14576
48. Cao J, Zhou Z, Song Q, Chen K, Su G, Zhou T et al (2020) Ultrarobust $Ti_{(3)}C_{(2)}T_{(x)}$ MXene-based soft actuators via bamboo-inspired mesoscale assembly of hybrid nanostructures. *ACS Nano* 14(6):7055–7065
49. Sedki M, Mirabedini PS, Nakama K, Stephens G, Groves M, Lee I et al (2022) Synthesis of pristine graphene-like behaving rGO thin film: insights into what really matters. *Carbon* 186:437–451
50. Liao C, Zhu X, Xie W, Zeng F, Yi S, Cheng H et al (2018) Solvent-assisted thermal reduction of microcrystalline graphene oxide with excellent microwave absorption performance. *RSC Adv* 8(28):15315–15325
51. Song J, Chen C, Yang Z, Kuang Y, Li T, Li Y et al (2018) Highly compressible, anisotropic aerogel with aligned cellulose nanofibers. *ACS Nano* 12(1):140–147
52. Kotal M, Kim H, Roy S, Oh IK (2017) Sulfur and nitrogen co-doped holey graphene aerogel for structurally resilient solid-state supercapacitors under high compressions. *J Mater Chem A* 5(33):17253–17266
53. Sun H, Xu Z, Gao C (2013) Multifunctional, ultra-flyweight, synergistically assembled carbon aerogels. *Adv Mater* 25(18):2554–2560
54. Wang C, Chen X, Wang B, Huang M, Wang B, Jiang Y et al (2018) Freeze-casting produces a graphene oxide aerogel with a radial and centrosymmetric structure. *ACS Nano* 12(6):5816–5825
55. Yang M, Zhao N, Cui Y, Gao W, Zhao Q, Gao C et al (2017) Biomimetic architected graphene aerogel with exceptional strength and resilience. *ACS Nano* 11(7):6817–6824
56. Zhuo H, Hu Y, Tong X, Chen Z, Zhong L, Lai H et al (2018) A supercompressible, elastic, and bendable carbon aerogel with ultrasensitive detection limits for compression strain, pressure, and bending angle. *Adv Mater* 30(18):1706705
57. Gao Y, Yan C, Huang H, Yang T, Tian G, Xiong D et al (2020) Microchannel-confined MXene based flexible piezoresistive multifunctional micro-force sensor. *Adv Funct Mater* 30(11):1909603
58. Li XP, Li Y, Li X, Song D, Min P, Hu C et al (2019) Highly sensitive, reliable and flexible piezoresistive pressure sensors featuring polyurethane sponge coated with MXene sheets. *J Colloid Interface Sci* 542:54–62
59. Long S, Feng Y, He F, Zhao J, Bai T, Lin H et al (2021) Biomass-derived, multifunctional and wave-layered carbon aerogels toward wearable pressure sensors, supercapacitors and triboelectric nanogenerators. *Nano Energy* 85:105973
60. Ma Y, Cheng Y, Wang J, Fu S, Zhou M, Yang Y et al (2022) Flexible and highly-sensitive pressure sensor based on controllably oxidized MXene. *InfoMat* 4(9):12328
61. Yu S, Li L, Wang J, Liu E, Zhao J, Xu F et al (2020) Light-boosting highly sensitive pressure sensors based on bioinspired multiscale surface structures. *Adv Funct Mater* 30(16):1907091

Publisher's Note Springer Nature remains neutral with regard to jurisdictional claims in published maps and institutional affiliations.